



The reflection and refraction of a curved shock front sliding over an air–water interface

R. Arun Kumar¹ · G. Rajesh² · G. Jagadeesh³

Received: 19 December 2021 / Revised: 20 June 2022 / Accepted: 21 July 2022 / Published online: 27 August 2022
© The Author(s), under exclusive licence to Springer-Verlag GmbH Germany, part of Springer Nature 2022

Abstract

The present study aims to investigate the reflection and refraction of a curved shock front as it slides along an air–water interface, using the time-resolved shadowgraph technique. The curved shock front is generated from a free-piston shock tube. The study successfully captured the propagation of a refracted shock wave in water along with that of the reflected shock wave in the air. The refracted shock moves much faster than the incident shock due to a higher acoustic speed in the water. It is seen that the reflected shock initially exhibits a regular reflection (RR), which then transitions to a Mach reflection (MR) as it propagates along the interface. As the shock wave propagates along the air–water interface, the incident shock wave angle with the interface keeps on increasing, leading to RR–MR transition. Shock polar analysis shows that as the Mach reflection structure propagates further along the interface, it transitions from a standard Mach reflection to a non-standard Mach reflection. It is seen that the distance the shock wave propagates along the interface before it transitions from RR to MR increases with the increase in the interface distance (distance between the water surface and the shock tube axis). It is also found that the reflection surface (water or solid) does not seem to have a significant effect on the shock transition criterion, especially the distance at which the shock wave transitions from RR to MR.

Keywords Air-water interface · Mach reflection · Unsteady shock wave reflection · Shock wave refraction · Shock wave transition

1 Introduction

The shock wave interaction with an interface and its subsequent reflection is one of the most critical fluid dynamic problems encountered in engineering applications with supersonic flows. Due to its immense practical importance, the shock wave reflection phenomenon over interfaces has been widely investigated in the past, especially with solid surfaces [1–3]. However, there are many practical situations in which the shock wave interacts with a liquid interface, such as an explosion over an ocean surface or an acciden-

tal explosion in liquid storage tanks. This is of particular interest to defense establishments such as battleships, where the shock loading (produced by a nearby explosion over the ocean surface or by gunfire) and the subsequent interfacial instabilities can cause collateral structural damage as well as stability issues. A proper understanding of shock reflection characteristics over the water surface will be useful in the design of many medical applications using shock waves as well since the acoustic impedance of water is nearly the same as that of human tissues [4].

It is to be noted that the shock wave interaction characteristics with a liquid surface are expected to produce profound changes compared to the interaction with a solid surface, mainly due to the lower acoustic impedance offered by liquid compared to solid. The most common difference is the formation of a prominent transmitted shock wave into the liquid surface compared to a solid surface [5], which may induce significantly large pressure levels in the liquid. The transmitted shock wave is generally termed as the refracted shock wave. Hence, the flow physics of shock wave interaction with an air–liquid interface is dominated by the dynamics

Communicated by A. Sasoh.

✉ G. Rajesh
rajesh@ae.iitm.ac.in

¹ Department of Mechanical Engineering, Indian Institute of Technology Jodhpur, Jodhpur, Rajasthan 342037, India

² Department of Aerospace Engineering, Indian Institute of Technology Madras, Chennai 600036, India

³ Department of Aerospace Engineering, Indian Institute of Science, Bangalore 560012, India

of the reflected as well as refracted shock waves, whereas, the flow physics of shock wave interaction with a solid surface is generally dominated by the dynamics of reflected shock wave alone.

In the literature, the shock wave reflection characteristics are broadly classified into two categories: (1) regular reflection (RR) and (2) an irregular reflection (IR, most commonly a Mach reflection MR), as shown in Fig. 1. The shock structures and other discontinuities for the two configurations are also shown in Fig. 1. The possible solutions of the shock structure (MR or RR) can be generally predicted from the pressure–deflection diagrams of the incident shock (*i*) and the reflected shock (*r*), commonly known as the *i*-polar and *r*-polar, respectively. From the *i*- and *r*-polars, the possible RR solution is the point where the *r*-polar meets the pressure axis, as shown in Fig. 1a. The possible MR solution is the point where the *r*-polar meets with the strong part of the *i*-polar (Fig. 1b). Classical shock wave studies have shown that for a particular shock upstream Mach number, there exists a critical shock wave angle at which RR transitions to MR (or vice versa), and based on this, several transition criteria were proposed. A detailed discussion regarding this can be found in the monograph by Ben-Dor [6].

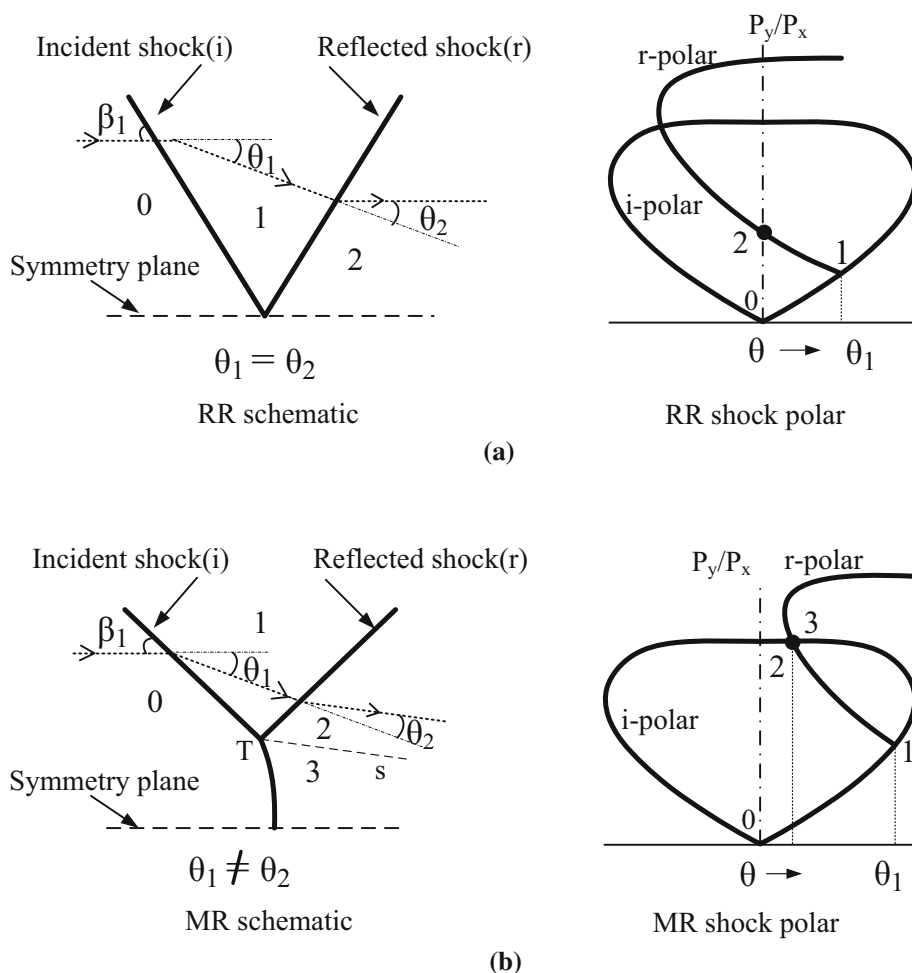
The shock wave reflection over a solid surface is a well-investigated research area, and there exists a good understanding of the transition criterion over various geometric surfaces [6–9]. However, there are still gray areas, especially on the shock reflection and its transition in unsteady flows where either the shock wave Mach number or the deflection angle or both continuously change with time. The complexity in predicting unsteady reflection arises from the fact that the reflected wave angle continuously changes owing to the constantly varying geometric surface or changing Mach number. Past studies on shock waves with a constant Mach number moving over a cylindrical concave surface reported that the shock structure transforms from a single Mach reflection (SMR) to regular reflection as it moves along the surface [6]. This transformation progresses through various complex Mach reflection structures such as transitional Mach reflection (TMR) and double Mach reflection (DMR) [6]. Similarly, the unsteady shock reflection over convex cylindrical surfaces also exhibits such complex shock reflection patterns [6]. Various analytical methods have also been proposed to predict the shock transition criteria for unsteady shock reflections over convex and concave surfaces [10–15]. In real life, the unsteady shock reflections are most commonly seen when a blast wave generated above the ground hits the ground and gets reflected while it propagates along the ground [16–18]. Unlike the unsteady reflection over convex and concave surfaces with constant Mach number, the blast wave reflection over ground is more complicated due to the continuously varying Mach number and wave angles. Hu and Glass [18] produced an extensive experimental database

on the blast wave propagation distance along the ground before it transitions from RR to various IR configurations (SMR, TMR, and DMR) for various explosion energies and heights of the burst. However, the physical understanding of the shock wave transition in such an unsteady scenario still received limited success.

It is thus seen from the literature that there are many studies in the past which investigated the shock reflection over solid surfaces. However, the shock reflection over the liquid interface has been scarcely investigated in the past. The major difference in shock wave interaction over the liquid surface compared to a solid surface is the existence of a refracted shock wave and surface instabilities. The analytical studies by Henderson et al. [19–21] proposed that the energy transfer by the refracted shock wave into the medium depends on the wave impedance in the medium. The analytical studies suggested that, for a shock wave interacting with an air–water interface, the majority of the shock energy would reflect due to the large wave impedance in water [19,20]. Hence, the refracted wave will be much weaker. Henderson [20] also reported that the refracted shock wave transitions from regular refraction to irregular refraction when the angle of the incident wave with respect to the interface is greater than a critical angle which is defined as the “intromission angle.” The study by Borisov et al. [22] reported that a plane shock front moving over a water layer produces a refracted shock wave which moves much faster than the incident shock wave due to the higher acoustic speed in water compared to air. As a result of this, a precursor shock wave originates from the higher density medium to the lower density medium [23,24]. Apart from the studies which investigated the shock refraction over the air–water interface, there were few studies that investigated the shock reflection characteristics [25–27]. One of the pioneering works in this regard is the research carried out by Takayama et al. [25] on shock wave reflections over water wedges. Their studies reported that the shock wave transition from regular to irregular reflections over water wedges matched well with the transition criteria based on the detachment condition of pseudo-steady flows (a plane moving shock wave over an inclined surface) over solid wedges. The study by Wan et al. [26] reported that the RR–MR transition (based on detachment condition) in pseudo-steady shock reflection over water wedges occurs at a smaller shock wave angle compared to the corresponding reflection over a solid surface. However, the variation is found to be very small. Other than the shock wave reflection over water wedges, there have been few studies in the past which investigated the reflection and refraction characteristics of a plane shock front over cylindrical water surface [28].

It is thus seen from the literature that, apart from a few experimental studies on shock reflection over water wedges and cylindrical water columns, the reflection characteristics of shock waves over an air–water interface have been largely

Fig. 1 Schematic showing RR and MR shock structure and their corresponding shock polars: **a** RR and **b** MR



unexplored. One of the major unattempted research areas is the unsteady reflection of a curved shock wave over a straight water surface. Even though the problem is similar to the blast wave reflection over the ground, it is expected that the reflection characteristics in the case of a water surface could be different due to the refracted shock wave and other surface instabilities. Moreover, the shock transition lines and various IR structures that could occur in purely unsteady shock reflection over the air–water interface have not been properly understood. It should also be noted that the classical studies on the refracted shock wave in the air–water interface were mostly analytically oriented with very few experimental works. In recent times, with the advent of ultra-high-speed imaging techniques, there have been few experimental studies that successfully visualized the complex shock reflection process, but limited success has been obtained in visualizing the refracted shock characteristics [29]. Hence, in this study, it is attempted to experimentally investigate the shock wave reflection and refraction characteristics when a curved shock front slides over an air–water interface. The transition conditions for RR to IR and the various possible IR configurations that could exist in the transition process for a purely

unsteady shock reflection over the air–water interface are also investigated. A comparative study of shock reflection characteristics of curved shock over solid and liquid surfaces is also presented.

2 Experimental setup

The curved shock front for the present study was produced by using a free-piston shock tube, which consists of three sections: (1) the high-pressure tube, (2) the pump tube, and (3) the launch tube, as shown in Fig. 2a. The high-pressure tube was separated from the pump tube using cellophane diaphragms (3 in number with a thickness of 0.1 mm each), and the pump tube was separated from the launch tube by the aluminum diaphragm (1.2 mm thick). The high-pressure tube was connected with a storage tank maintained at 25-bar pressure. The pressure in the high-pressure tube builds up when the air from the storage tank was delivered to the high-pressure tube. At a critical pressure ratio, the diaphragm breaks and produces a shock wave that propagates into the pump tube. In the pump tube, a metallic piston of a diameter of 59 mm was kept close to the cellophane diaphragm.

The unsteady shockwave in the pump tube pushes the piston, which compresses the pump tube air and generates very high pressure in the pump tube. The compressed air upstream of the piston gives a force in the opposite direction to the piston motion and may eventually stop the piston motion depending on the geometric design of the tube. The high pressure generated in the pump tube breaks the aluminum diaphragm and produces a very strong shock wave that moves into the launch tube. The so-produced shock front, when it comes out of the launch tube, diffracts and produces a curved shock front. Toward the end of the launch tube, a tank filled with water was placed. A sufficiently large water tank (50 cm length \times 50 cm width \times 40 cm height) was chosen for the present study to avoid the effect of shock wave reflections from the sidewall. Plexiglas windows (20 cm length \times 15 cm height \times 1 cm thickness) were provided at the sidewalls for visualization purposes. Four experimental cases were conducted in the present study. Case-1, case-2, and case-3 were carried out with the water tank kept at the tube exit with the water surface maintained at a distance of 60 mm, 45 mm, and 30 mm, respectively, below the launch tube axis. Case-4 is carried out by placing a solid surface made of mild steel at the top side of the tube exit (with the solid surface maintained at a distance of 58 mm above the launch tube axis) and the water surface on the bottom side (with water surface maintained at a distance of 58 mm below the launch tube axis), as shown in Fig. 2b. The distance between the water surface and the shock tube axis is termed as the “interface distance.” The details of the test cases are shown in Table 1. In the present study, the shock wave propagation was visualized using time-resolved shadowgraph imaging. The experiments were repeated several times for error analysis.

It should be noted that for each of these experiments, the recording speed (in frames per second, fps) and resolution were different. However, a minimum of 150,000 fps was maintained for all the experiments, with some experiments being conducted at around 200,000 fps. Images were captured using an IX-726 camera at 289-ns exposure. In the present study, a halogen light source of Newport make was used to illuminate the test area. A condensing lens was used to create a converging light beam from the light source which falls on the slit to generate an extended image of the light source. The focal length of the condensing lens is 50 mm with the f-number equal to 1. The light is collimated by the first field mirror (concave mirror of 300 mm diameter and 2000 mm focal length). The distance of the camera from the tank varies with the lens parameters. The f-number of the camera lens was 2 (fast lens) with a focal length of 100 mm. The sensitivity of the shadowgraph is changed by changing the distance of the second mirror from the test section. This would eventually change the deflection length of the light beam due to the density gradients, which is a measure of the sensitivity of the shadowgraph system.

The free-piston shock tube used for the present study does not have any mechanisms for externally controlling the diaphragm breaking process, such as a diaphragm puncturing mechanism using a needle or quick opening valve. As a result of this, a predetermined pressure ratio cannot be maintained across the high-pressure tube and the pump tube. Nevertheless, the repeatability of the pressure ratio can be guaranteed by using diaphragms with the same thickness and cross-section area, since the pressure ratio is determined by the diaphragm breaking pressure. The repeatability of the pressure ratio conditions for various experiments is also checked by measuring the pressure jump on the downstream side of the launch tube. Three PCB piezoelectric sensors were mounted on the launch tube for measuring the shock pressure jump, as shown in Fig. 3a. The sensitivity of the sensors used is 0.145 V/bar (10 mV/psi). The voltage signals from the pressure sensors are amplified with a gain factor of 2. The new sensitivity, therefore, becomes 0.29 V/bar. Pressure data were acquired at a sampling rate of 150 kHz. Figure 3b shows the pressure histories from the three PCB sensors for the case-1 experiment. The pressure histories were calculated from the voltage signals from the sensors. The pressure measurements were also carried out for other experimental cases, and the initial shock pressure jump at the launch tube for various cases is reported in Table 1. The voltage signals (or the pressure signals) from the sensors were also used to compute the initial shock Mach number. The sharp pressure rises in Fig. 3b indicate the arrival of the shock wave at each of the sensors, which were mounted at a gap of 150 mm. The time interval taken by the shock wave to cross over the sensor locations can be easily found in Fig. 3b, and this can be used to compute the shock speed, which in turn can be used to compute the shock Mach number. The computed shock wave Mach number from Fig. 3b is 3.730 ± 0.091 . Similarly, the initial shock wave Mach numbers for other experimental cases were also measured from their corresponding voltage signals and are reported in Table 1. It is evident from the pressure measurements in the launch tube that the initial shock wave Mach number is nearly the same for all the cases, which ensures the uniformity of the experiments.

3 Results and discussion

This section consists of two parts. The first part discusses the unsteady shock reflection and refraction characteristics over the liquid surface, and the second part compares the shock reflection characteristics over solid and liquid surfaces.

3.1 Unsteady shock wave reflection and refraction over plane liquid surface

Figure 4 shows the shadowgraph images depicting the early evolution of the shock structure outside the shock tube. It

Fig. 2 Experimental setup: **a** shock propagation over air–water interface and **b** shock propagation over solid and liquid surface

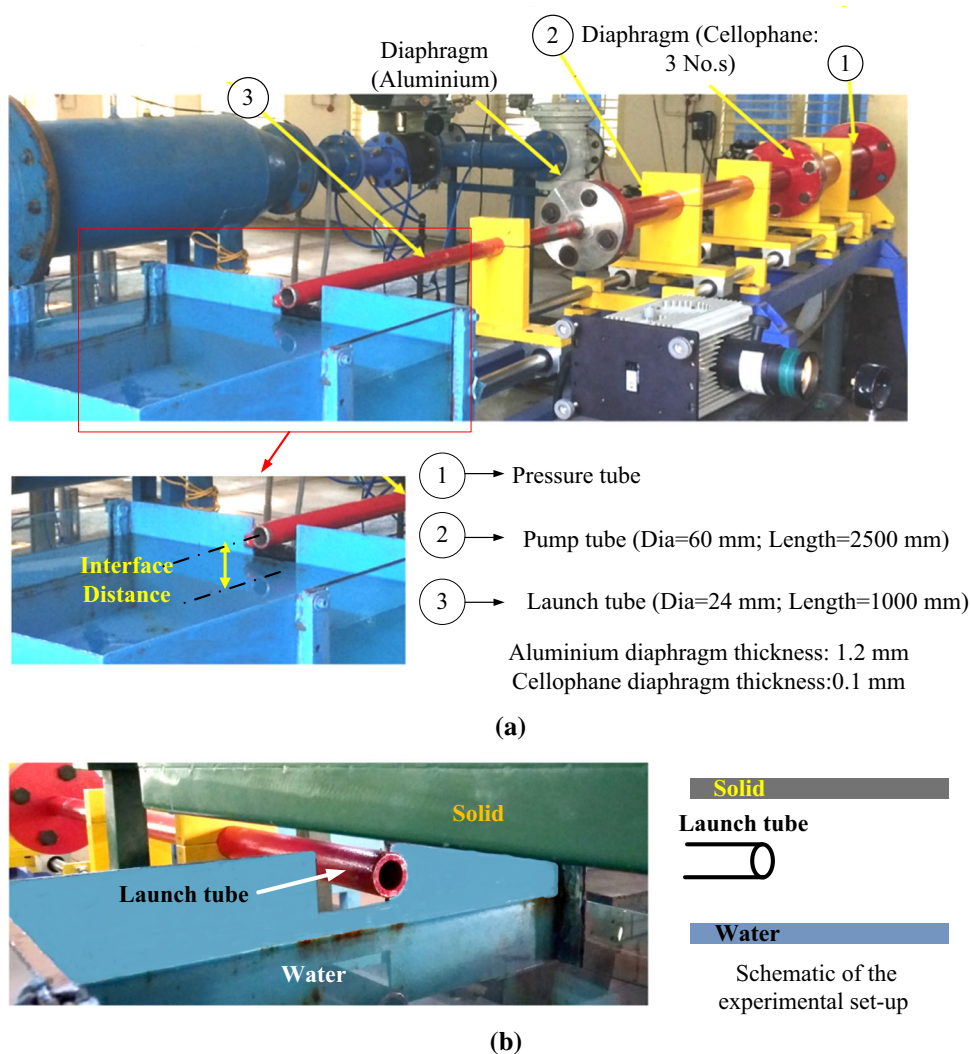


Table 1 Various experimental cases

Cases	Interface distance (<i>h</i>) [mm]	Shock interaction surface	P_2/P_1	M_{init}
1	30	Water	15.82 ± 0.74	3.730 ± 0.091
2	45	Water	14.66 ± 0.73	3.680 ± 0.103
3	60	Water	14.59 ± 0.47	3.600 ± 0.083
4	58	Solid (mild steel) on top and water on bottom	14.67 ± 0.44	3.690 ± 0.054

is seen from the shadowgraph images that the shock front diffracts and becomes curved as soon as it comes out of the shock tube. During the initial stages of shock evolution outside the shock tube, the shock front remains plane near the shock tube axis. During this period, the shock diffraction is more prominent toward the edges of the shock front, as shown in Fig. 4a–c. As the shock front moves further downstream, it attains a nearly spherical front as shown in Fig. 4c–d. In the shadowgraph images in Fig. 4, two distinct lines can be observed at the plexiglass edge in the air side. These lines

are due to the parallax error in visualization and not due to any flow features.

Figures 5, 6, and 7 show the shadowgraph images of the curved shock wave interaction with the air–water interface and its subsequent propagation characteristics over the interface for the case-1, case-2, and case-3 conditions, respectively. It is well known that when the shock front interacts with the air–water interface it produces reflected as well as refracted shock waves [5]. However, it was reported that only a small fraction of the incident shock energy will be transferred to the refracted shock wave in water, and

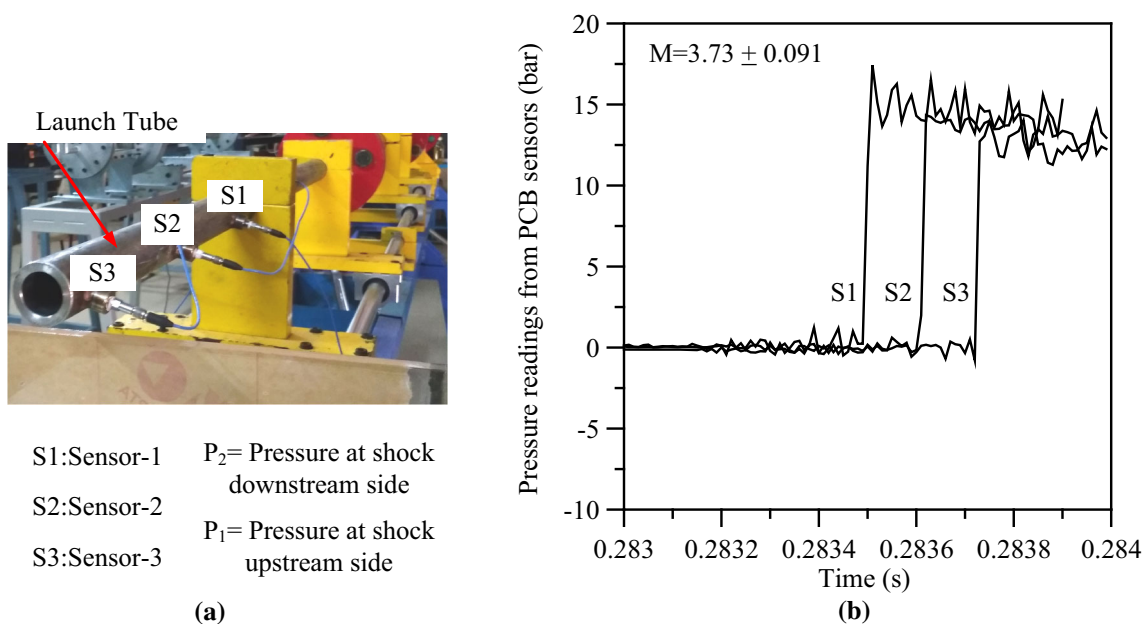


Fig. 3 Pressure measurements in the launch tube: **a** sensor locations and **b** pressure readings from various sensors

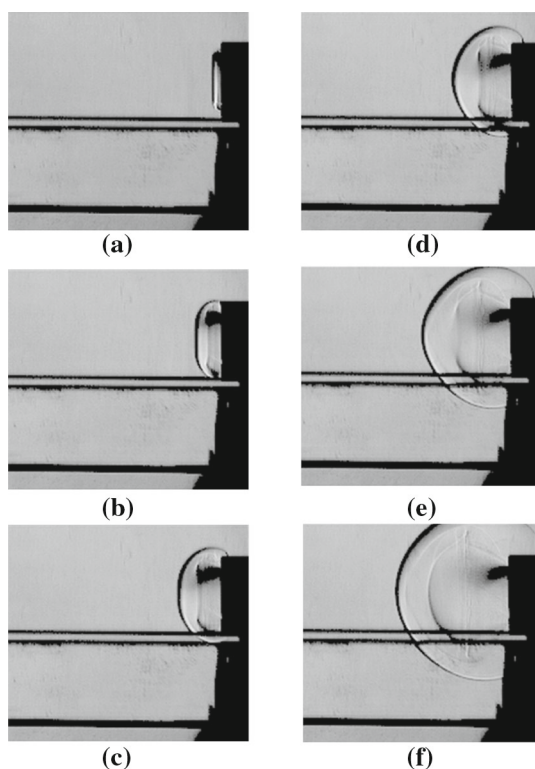


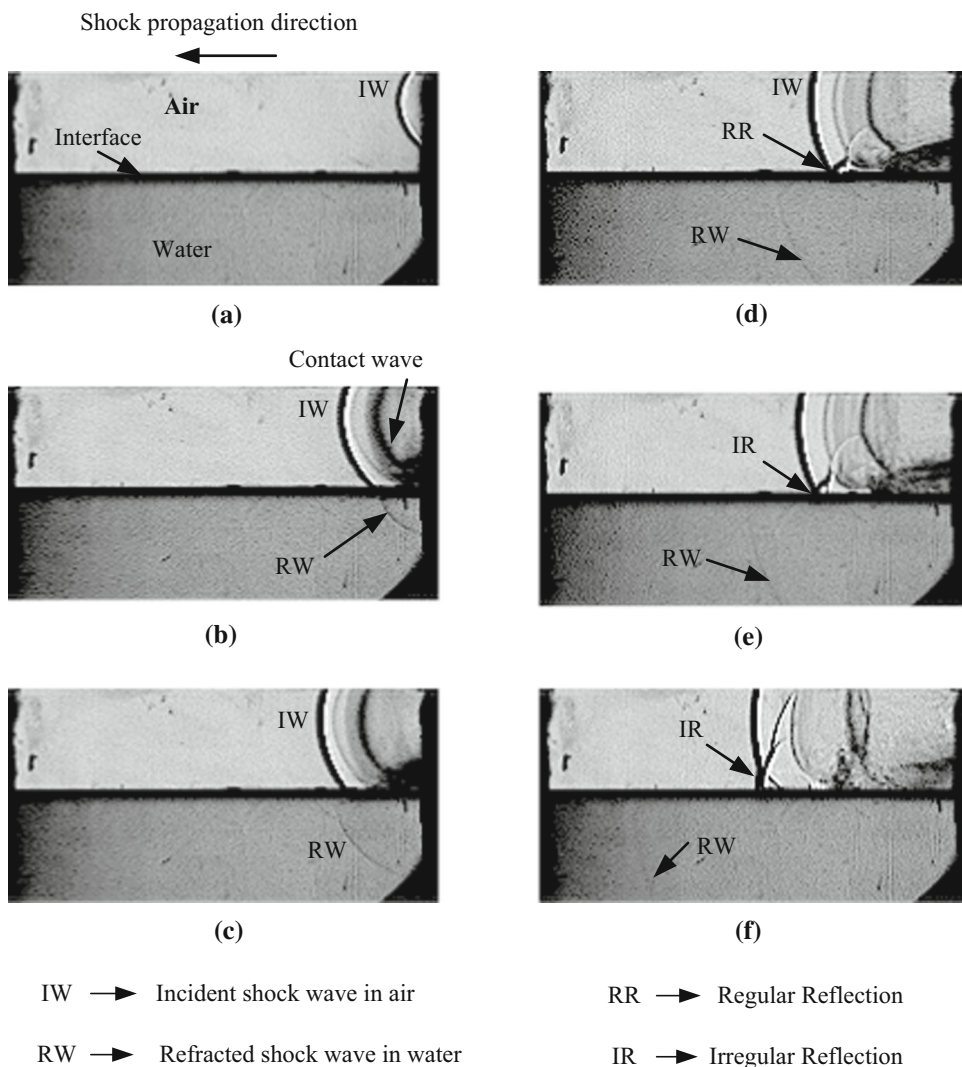
Fig. 4 Shadowgraph images showing the early evolution of shock wave from the launch tube (case-2): **a** $t = 0 \mu\text{s}$, **b** $t = 6.667 \mu\text{s}$, **c** $t = 13.33 \mu\text{s}$, **d** $t = 20 \mu\text{s}$, **e** $t = 33.33 \mu\text{s}$, and **f** $t = 46.67 \mu\text{s}$

therefore, the strength of the refracted shock will be quite weak compared to the incident shock in the air [26,29]. As a result of this, many past experiments were not success-

ful in visualizing the refracted wave, and it was concluded that the refracted wave soon degenerates into compression waves as it propagates through water [26]. However, the high-speed time-resolved shadowgraph images from the present study clearly show the propagation of a sharp-wave discontinuity into the medium (Fig. 5b–e for case-1 and Fig. 6b–c for case-2). The refracted wave is not observed in Fig. 7, as the sensitivity of the shadowgraph was purposefully reduced to eliminate the noise, in order to capture the characteristics of the reflected wave. The refracted wave moves faster than the incident wave due to the larger acoustic speed in water compared to air. It is also found that the refracted wave travels as a shock discontinuity for a reasonably large distance inside the water (Fig. 5). From the shadowgraph images (Figs. 5 and 6), it can also be seen that the refracted shock wave pixel intensities are very feeble. Hence, a quantitative estimation of refracted shock propagation is found to be difficult in the present study and only qualitative visualization is reported. It should also be noted that there should exist a series of precursory waves ahead of the incident shock wave over the water surface due to the large difference in acoustic impedance ($Z = \rho c$, where ρ is the density of the medium and c is the acoustic speed in the medium) across the air–water interface (the ratio of acoustic impedances between air and water is 2.8×10^{-4}) and in air–solid interface (the ratio of acoustic impedances between air and solid is 1.25×10^{-5}). However, in the present study such precursory waves are weak to be seen and can be neglected in the induced pressure field.

The shadowgraph images (Figs. 5, 6, and 7) also show that the reflected shock wave exhibits regular reflection (RR)

Fig. 5 Shadowgraph images of the curved shock wave reflection and refraction as it slides over an air–water interface (case-1). Here time $t = 0$ refers to the time instant at which the shock just comes out of the shock tube: **a** $t = 10 \mu\text{s}$, **b** $t = 45 \mu\text{s}$, **c** $t = 60 \mu\text{s}$, **d** $t = 90 \mu\text{s}$, **e** $t = 100 \mu\text{s}$, and **f** $t = 140 \mu\text{s}$



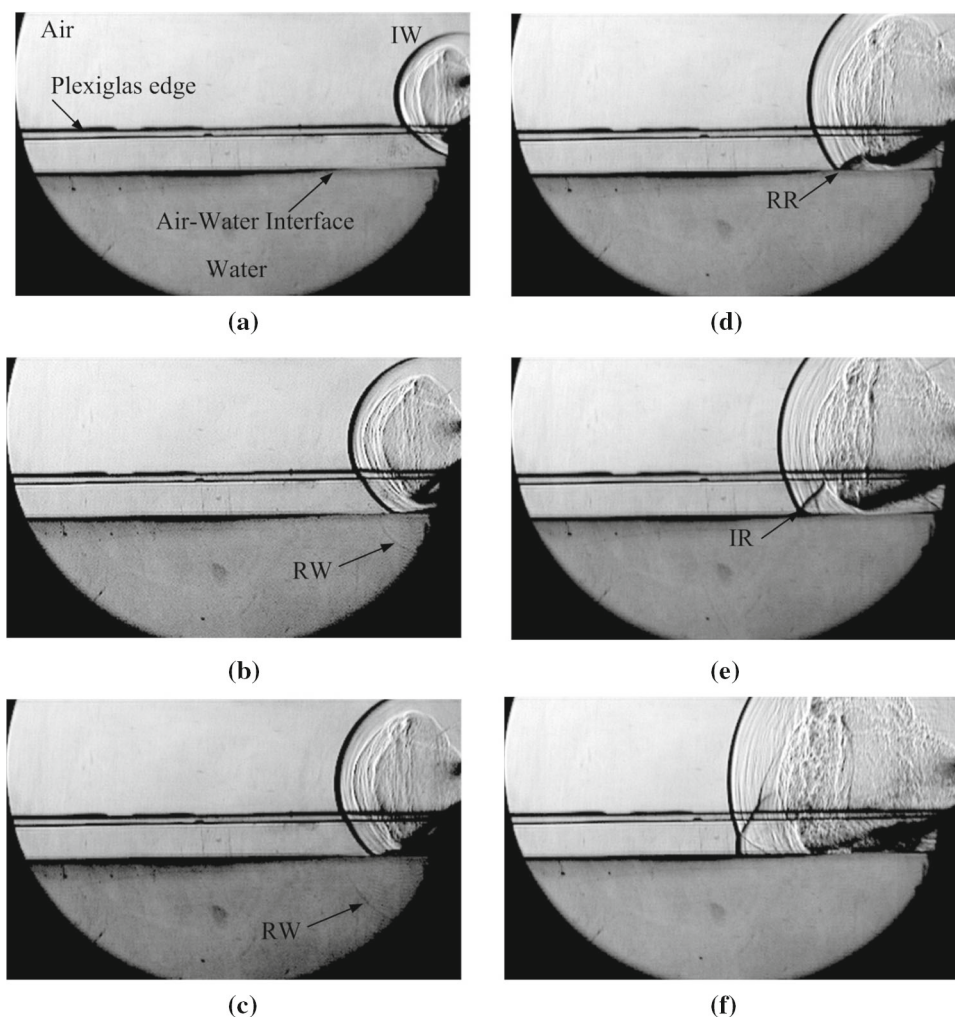
as soon as it interacts with the liquid interface. As it propagates along the interface, the regular reflection transitions to an irregular reflection, IR (most commonly, a Mach reflection, MR). These transitions can be seen in Figs. 5d–e, 6d–e, and 7d–e.

It should be noted that the present experiment is a purely unsteady shock reflection phenomenon since the shock wave angle with the interface increases and the incident shock Mach number decreases as the shock propagates downstream along the interface. This is an unfavorable condition for the existence of the RR shock structure, and at a critical shock wave angle, the shock structure transitions to IR. In order to find the transition angles for RR to IR with various interface distance cases or the curvatures of the shock wave, the shock wave angle at the transition point was computed from the shadowgraph images using image processing. An edge detection algorithm was used to track the shock front from the images, and the shock wave angles at each time instant were computed by reconstructing the incident shock front

from the pixel distributions at the shock front (details of the image processing and measurement procedures are given in the Appendix). Experiments were repeated (at least three times) for each of the water-level cases to check the repeatability and errors associated with the measurement. The error in the shock wave angle at transition was computed from the standard deviation of the measured values from various experiments conducted for a particular water-level experiment. The details of error estimation are also given in the Appendix.

Figure 8a shows a schematic representation of the initial wave angle and the wave angle at transition. The shock wave will be parallel to the interface when it first interacts with the water surface. However, soon after the interaction of the incident shock wave with the water surface, a reflected shock wave is produced. As the incident shock wave propagates upstream, the shock wave subtends a positive angle with the interface. The initial shock wave angle is, therefore, defined as the wave angle corresponding to the time instant at which

Fig. 6 Shadowgraph images of the reflection and refraction of a curved shock as it slides over the air–water interface (case-2). Here time $t = 0$ refers to the time instant at which the shock just comes out of the shock tube: **a** $t = 53.33 \mu\text{s}$, **b** $t = 86.67 \mu\text{s}$, **c** $t = 100 \mu\text{s}$, **d** $t = 133.33 \mu\text{s}$, **e** $t = 153.33 \mu\text{s}$, and **f** $t = 220 \mu\text{s}$



the tracing of the angle has been started. The shock wave angle tracking has commenced from the very next frame after the shock wave interacts with the water surface. In the present study, the transition point is identified as the image just prior to the image where a noticeable Mach stem is observed. This is because the determination of the exact transition point from the images is very difficult since, at the inception point of transition, it is highly likely that the Mach stem is embedded inside the dark zone produced by the air–water interface.

Figure 8b shows the variations of the initial wave angle and the wave angle at transition for various interface distance cases. It is seen from Fig. 8b that even though the initial shock wave angle is significantly different, the wave angle at shock transition is more or less the same within the error limit. It should be noted that these conclusions are based on the pixel values from the images and are subject to an uncertainty corresponding to the physical distance represented by ± 0.5 pixels. For the present case, the image resolution is not very high (440×220 pixels) owing to the high fps required to capture the reflected and refracted shock waves, and as a

result of this, the error from pixel computation is relatively large (see the Appendix for details). Nevertheless, the results show that even with significant variation in the water level from the shock tube axis, the transition angle for RR to IR does not seem to vary largely and is lying in close ranges.

A qualitative picture of the aspects discussed above can be obtained from the shadowgraph images for the various cases, as shown in Fig. 9. Figure 9a–c shows the shock wave angles with the interface for various cases at the onset of shock interaction with the interface, and Fig. 9d–f shows the shock wave angles at the onset of RR to IR transition. It is clear from Fig. 9a–c that the initial shock wave angle decreases with the increase in water level. However, the shock wave transition occurs when the shock wave angle reaches nearly the same value for all the cases with various interface distance (Figs. 8b and 9d–f).

A constant shock wave angle at the transition point indicates that the incident shock wave Mach number at transition should also be the same for all the cases. In order to further investigate this, the incident shock wave Mach number along

Fig. 7 Shadowgraph images of the reflection of a curved shock as it slides over the air–water interface (case-3). Here time $t = 0$ refers to the time instant at which the shock just comes out of the shock tube:
a $t = 53.33 \mu\text{s}$, **b** $t = 93.33 \mu\text{s}$,
c $t = 133.33 \mu\text{s}$,
d $t = 173.33 \mu\text{s}$, **e** $t = 220 \mu\text{s}$,
f $t = 273.33 \mu\text{s}$

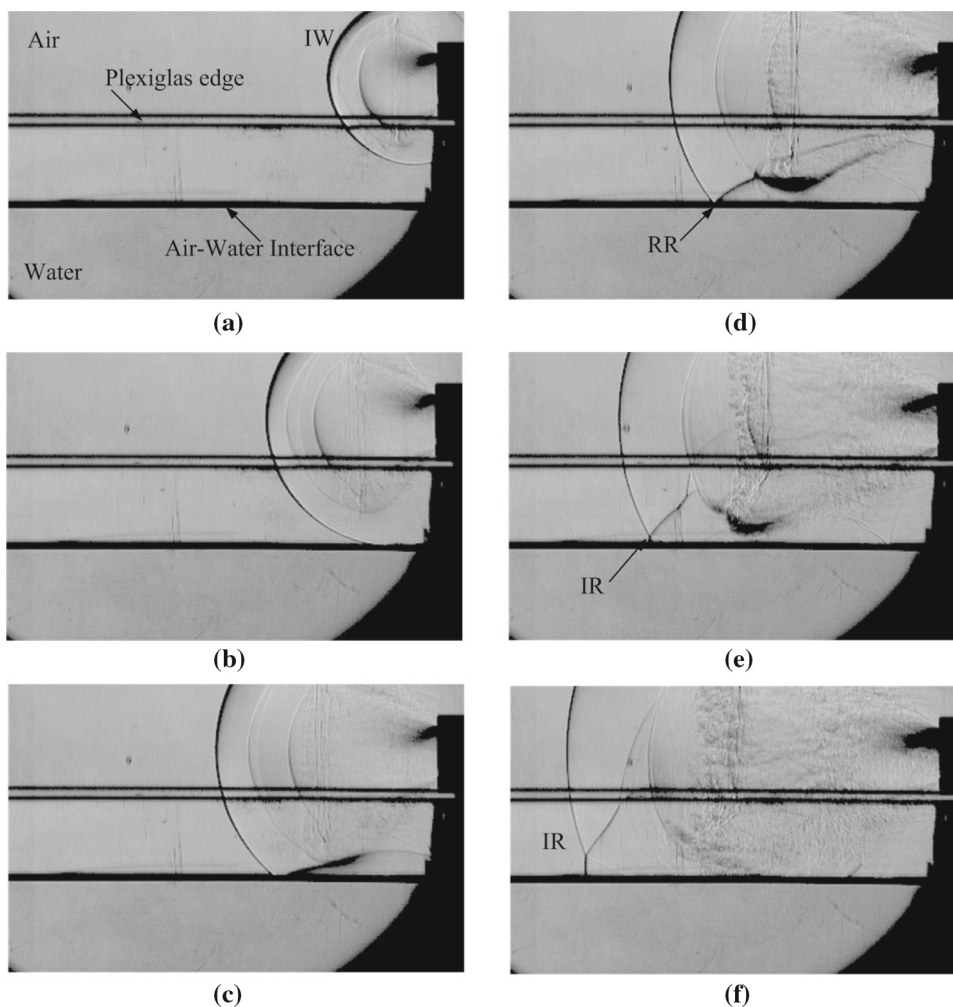


Fig. 8 Initial and transition shock wave angle with the interface at various time instants for the three cases with various water heights: **a** schematic showing initial and transition shock wave angles and **b** initial and transition shock wave angles

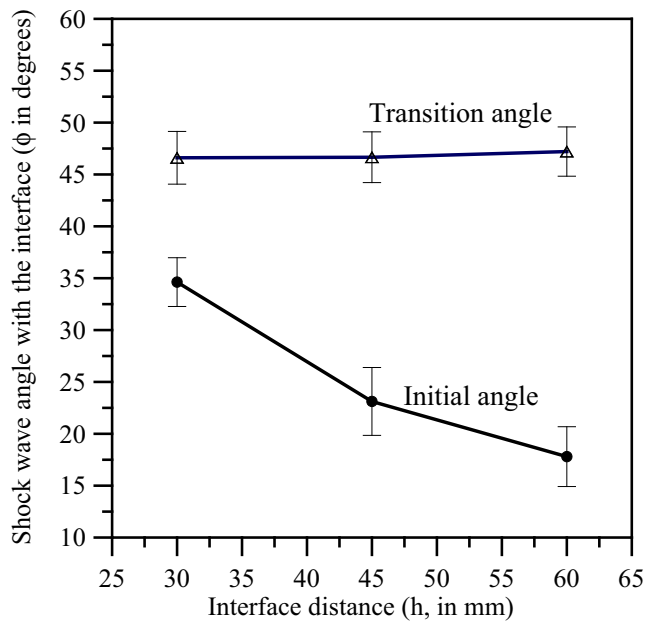
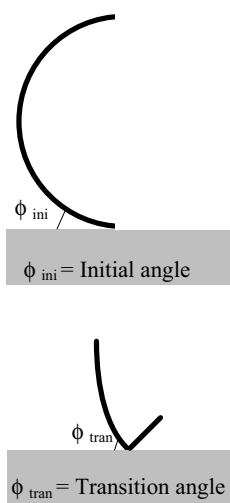
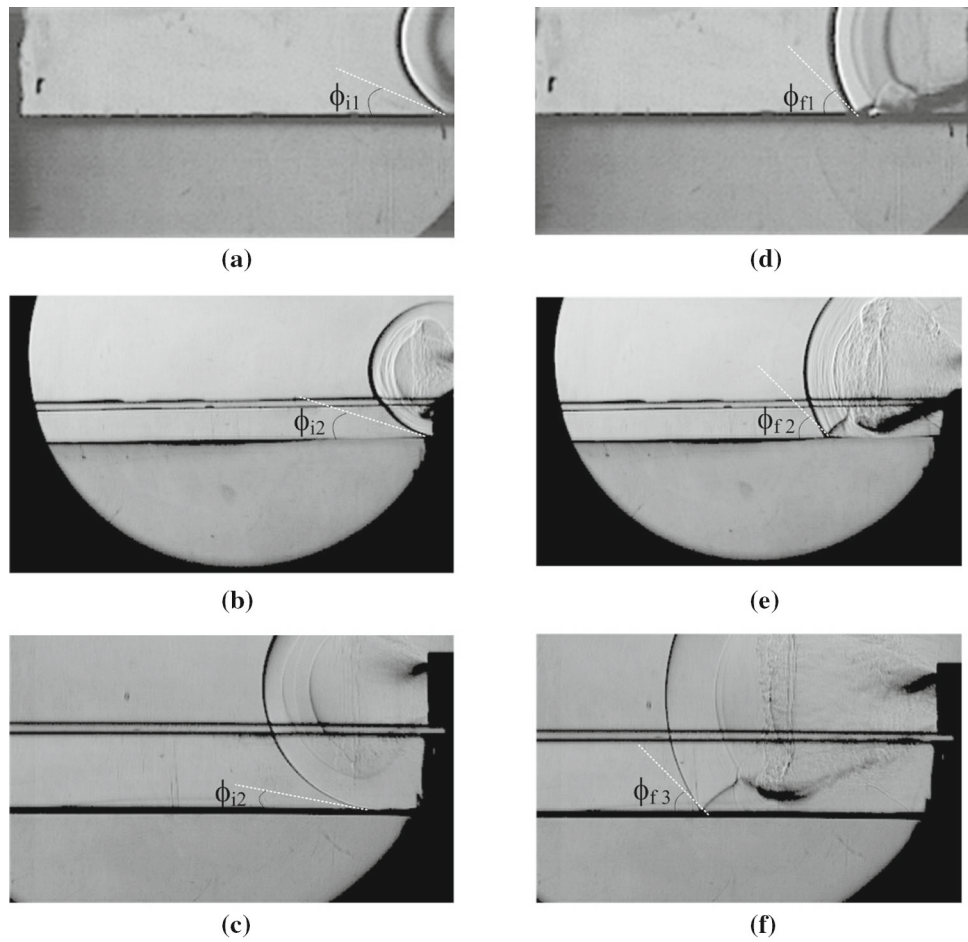


Fig. 9 Shadowgraph images showing the initial and transition shock angles with the interface for the three cases with various water heights: **a** initial shock wave angle for case-1, **b** initial shock wave angle for case-2, **c** initial shock wave angle for case-3, **d** transition shock wave angle for case-1, **e** transition shock wave angle for case-2, and **f** transition shock wave angle for case-3



$$\phi_{i1} > \phi_{i2} > \phi_{i3}$$

$$\phi_{f1} \approx \phi_{f2} \approx \phi_{f3}$$

ϕ_i → Initial Shock angle with interface

ϕ_f → Shock angle with interface at the onset of RR to MR transition

the interface was tracked for all the cases and is shown in Fig. 10. A detailed discussion on the Mach number computation from images is given in the Appendix. Figure 10 shows that, even though the initial shock strength inside the shock tube is more or less the same for all the cases (Table 1), the incident shock wave Mach number at the interaction point with the interface increases with the decrease of interface distance. This is because, for a larger interface distance (case-3) the shock wave has to travel more distance before it interacts with the water surface and the shock energy lost due to the diffraction effects is more. This essentially means that the shock wave Mach number at the interaction point with the interface is higher for a smaller interface distance (case-1) compared to the larger interface distance (case-3).

The Mach number plot also shows that the incident shock Mach number reduces rapidly due to the shock attenuation for all the cases as the shock propagates along the interface, which is similar to the typical exponential shock decay that

can be seen in an explosion. It is also seen that the Mach number for all the cases decays to nearly the same value at the transition point. It should also be noted that the initial shock wave angle is larger when the distance between the shock tube end and the interface is smaller (see the images in Fig. 9a–c). This is because the radius of the initial curved shock, while it interacts with the interface, is smaller when the distance between the shock tube axis and the interface is small. As a result of this, the initial shock front exhibits a larger curvature and hence a larger shock wave angle at the interaction point.

On the other hand, with the increase in the distance between the shock tube axis and the water surface, the radius of the shock wave grows further (smaller curvature and slope at the interaction point), resulting in a reduction in the shock wave angle when it interacts with the interface. A schematic representation of this is shown in Fig. 11a. As the shock front propagates along the interface, the shock angle keeps

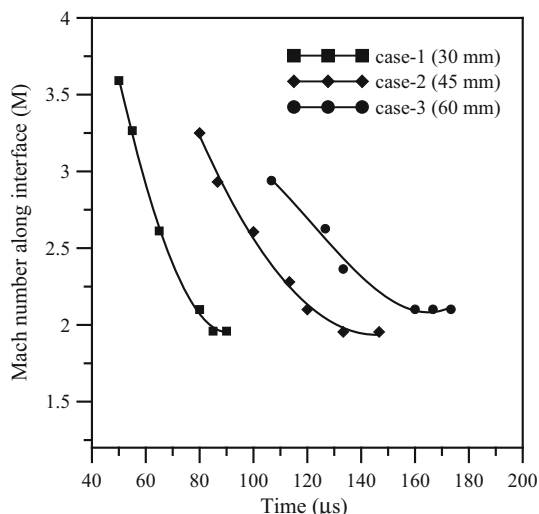
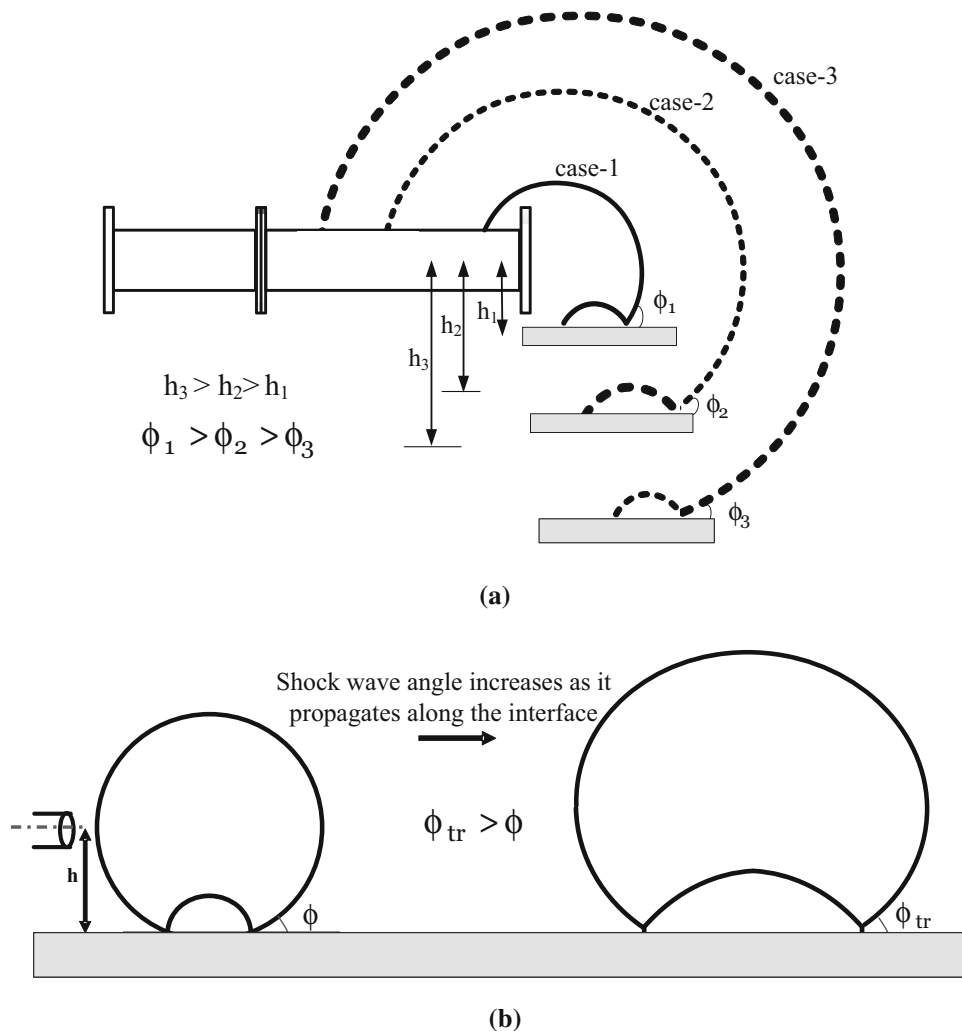


Fig. 10 Mach number variation along the interface for the three cases with various interface distance. Error in Mach number computation from image processing is ± 0.162 . Here, the first symbol of each data series corresponds to the time instant at which the shock front comes in contact with the interface for the first time

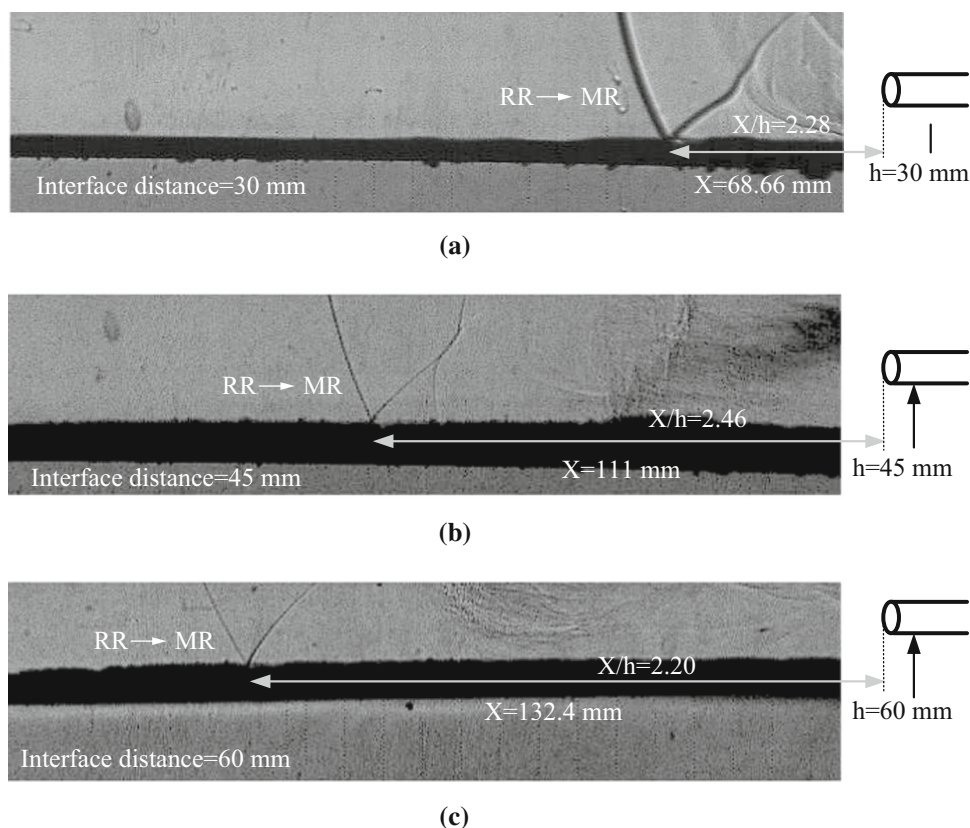
Fig. 11 Schematic of shock wave angle variations: **a** initial shock wave angle variation with change in the interface distance and **b** shock wave angle variation during the shock propagation along the interface



on increasing (as shown schematically in Fig. 11b). Hence, for a smaller initial shock wave angle (case with a large distance between the shock tube and interface), the shock front needs to travel more distance to reach the transition shock angle when compared to the case with a larger initial shock angle (case with a smaller distance between the shock tube and interface) as shown in Fig. 11a and b. Since the incident Mach number decreases and the wave angle increases as the shock propagates along the interface, the Mach number downstream of the incident shock wave decreases continuously, leading to a continuously increasing flow deflection angle. This results in a situation where the fluid condition downstream of the incident shock (region-1 in Fig. 2) is approaching the detachment condition corresponding to a particular Mach number, and results in RR–IR transition.

It is also seen that the shock wave attenuates much more rapidly for the smaller interface distance case compared to the larger interface distance case, as shown in Fig. 10. A much faster attenuation for the smaller interface distance compared to the larger interface distance is probably due to

Fig. 12 Shadowgraph images showing the shock propagation distance from the shock tube end when it transforms from RR to MR for various water heights: **a** case-1, **b** case-2, and **c** case-3



the larger initial Mach number at the onset of interaction with the water surface for the former case compared to the latter. A higher incident shock Mach number decay and a higher shock wave angle at the onset of interaction for the smaller interface distance case result in a situation where the transition occurs much faster for the smaller interface distance case compared to the larger interface distance case. With the increase in the interface distance, the shock wave angle at the onset of interaction is much smaller compared to the smaller interface distance case. Moreover, the incident shock Mach number attenuates slowly for larger interface distance case. In the present experiments, the variation in the decay rate of the Mach number and the growth rate of the wave angle for various cases occur in such a way that a common transition point (transition Mach number and wave angle) is attained for the different cases as the shock propagates along the interface. It should also be noted that the present experiments employ image processing methods to arrive at the quantitative results. These derived results might result in more error in the measurements compared to direct flow field measurements, such as using pressure sensors. Nevertheless, considering the difficulty in the direct flow field measurement along the interface (for example, placing a pressure sensor at the interface would contaminate the shock structures and hence meaningful measurements would not be possible), the

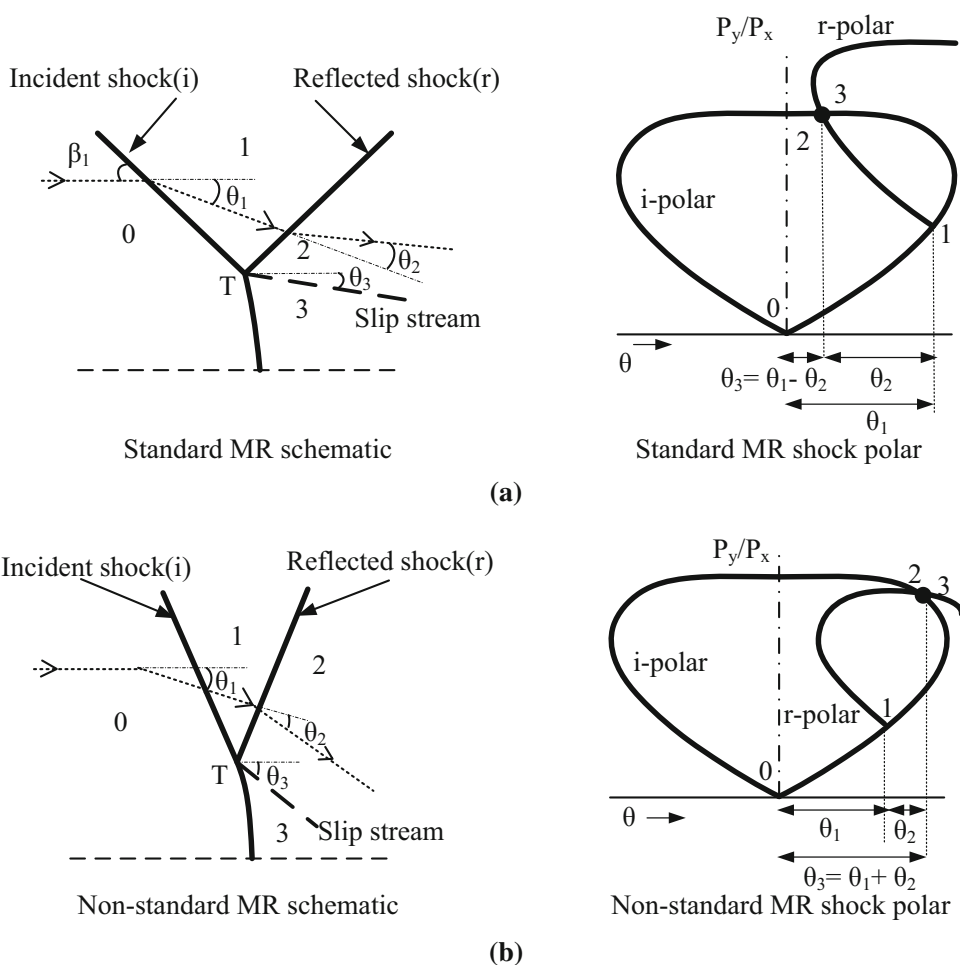
results from the images provide a first-hand estimate of the flow field.

The smaller initial angle at the onset of interaction and slower decay of incident Mach number for the larger water-level case result in a situation where the transition conditions are attained with a much longer propagation distance along the interface, with an increase in the interface distance. This is evident from Fig. 12, which shows the shadowgraph images of the shock transitions for the three cases with various interface distances. The shadowgraph images shown in Fig. 12 are from a new set of experiments carried out under the same conditions, in which the shock reflection area is zoomed in, and the images were captured at a higher frame rate of 196,540.

3.1.1 Characteristics of irregular shock reflection

A careful observation of the shadowgraph images shows that the shock reflection eventually resembles a non-standard reflection. The classification of standard and non-standard reflection is based on the net deflection angle produced by the reflected shock wave, as shown schematically in Fig. 13. In Fig. 13, the incident shock wave angle is represented as “i” and the reflected shock wave as “r” with θ_1 and θ_2 representing the flow deflection angles for the incident and reflected shocks, respectively. A standard-type reflection occurs, if the net deflection produced by the incident and reflected shocks

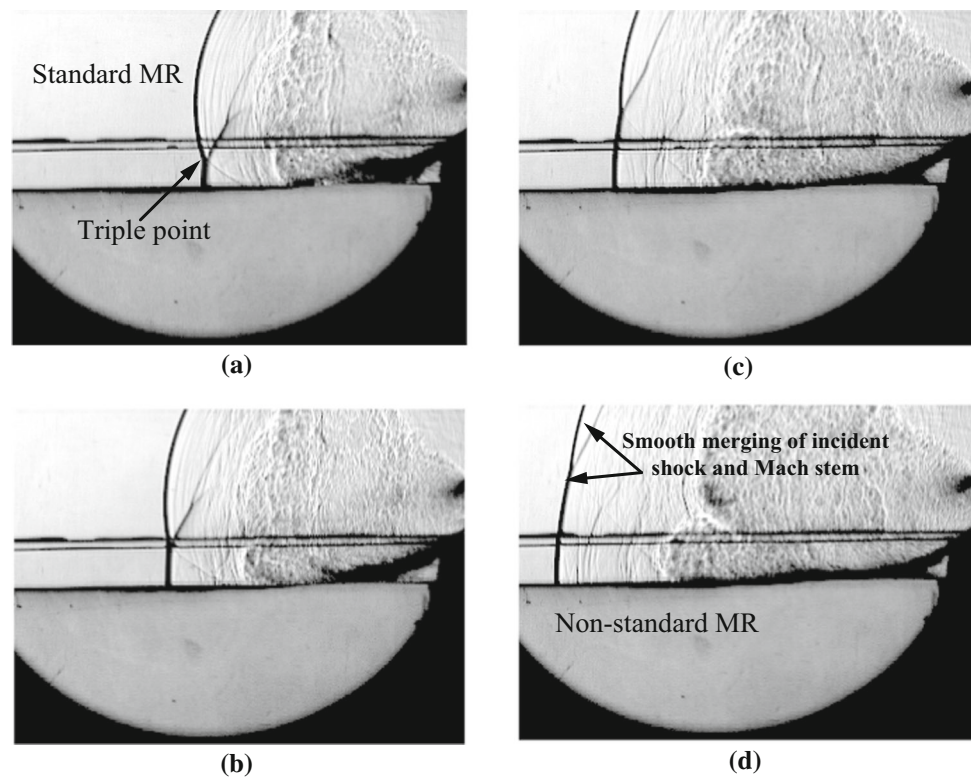
Fig. 13 Schematic showing standard and non-standard MR shock structure and their corresponding shock polars: **a** standard MR and **b** non-standard MR



is such that the slipstream angle (θ_3) will be $\theta_3 = \theta_1 - \theta_2$. Whereas, a non-standard-type reflection occurs when the net deflection is such that the slipstream angle is given by $\theta_3 = \theta_1 + \theta_2$. Alternatively, for standard Mach reflection, the flow deflection after the reflected shock wave will be opposite to the direction in which the flow deflected after the incident shock wave and for non-standard reflection both incident and reflected shock wave deflect the flow in the same direction. Schematics of the flow structure and shock polar for standard and non-standard Mach reflections are shown in Fig. 13a and b, respectively. Ben-Dor [6] reported that a non-standard reflection, in general, exhibits feature such as a smooth merging of incident shock with the Mach stem. The shadowgraph images (Fig. 14d) of the irregular shock reflection propagation characteristics for the case with a water level of 45 mm depict that the shock structure closely resembles that of a non-standard shock structure with the smooth merging of incident shock with the Mach stem. This essentially means that the irregular shock wave reflection transitions from a standard Mach reflection to non-standard Mach reflection (Fig. 14).

To further investigate the transition of standard Mach reflection to non-standard Mach reflection as the IR wave propagates along the interface, a shock polar analysis was carried out. For unsteady or pseudo-steady reflections, the shock polar must be drawn with the Mach number of the triple point moving along the triple-point trajectory and with the wave angle based on the triple-point trajectory [6]. This essentially means that the present analysis has to be carried out with a coordinate system fixed at the triple point and moving along the triple-point trajectory. A schematic of this is shown in Fig. 15a. The coordinate transformation was done by tracking the triple-point location (T) at various time instants from the shadowgraph images and computing the triple-point trajectory angle (χ) with respect to the air–water interface (horizontal direction). From the images, the incident shock wave angle with the horizontal (ϕ_s), as well as the Mach number of the triple point along the horizontal direction (M_s) at various time instants, was also computed. From this information, the Mach number of the triple point along the triple-point trajectory (M_0 —the flow Mach number in the triple-point fixed coordinate system) as well as the shock wave angle with respect to

Fig. 14 Shadowgraph images showing the transition from standard to non-standard-type Mach reflection (case-2): **a** $t = 180 \mu\text{s}$, **b** $t = 213.33 \mu\text{s}$, **c** $t = 246.67 \mu\text{s}$, and **d** $t = 346.67 \mu\text{s}$



triple-point trajectory can be computed, as shown in Fig. 15a. The details of the computation of various angles are given in the Appendix.

Figure 15b–d shows the shock polars for the case with an interface distance of 45 mm at various time instants. The shock polar in Fig. 15b clearly shows that the shock reflection exhibits a regular reflection. The shadowgraph image at the same instant (shown as an inset in Fig. 15b) also shows a regular reflection pattern. At a later time, the shock structure transitions to an irregular reflection as a single Mach reflection (SMR) with standard solution. This can be noticed from the shock polar, and the shadowgraph image is shown in Fig. 15c. As the shock front moves further, the reflection pattern exhibits a non-standard Mach reflection pattern. This can be clearly observed from the shock polar, and the shadowgraph image is shown in Fig. 15d. Thus, the shock polar analysis confirms that the curved shock reflection over an air–water interface structure eventually becomes a non-standard Mach reflection. The shadowgraph images for different water-level cases (Fig. 16) show a smooth merging of incident shock with the Mach stem which is a typical characteristic of non-standard reflection [6]. Hence, from Fig. 16 also it is evident that the shock structure eventually transitions to a non-standard Mach reflection for all the cases. It can be noticed that the Mach number of the curved shock at the transition condition is less than 2.202 in all the cases investigated, which indicates that the shock reflections occur in the weak reflection domain [6]. The fact that the RR tran-

sitions to IR lead to the possibility that the IR can be a vNR [30] (von-Neumann reflection), a VR [31] (Vasilev reflection), or a GR [32] (Guderley reflection). It is, however, not attempted in the present work to classify the reflections into the above types, as the error in the angles measured is larger than the difference in the shock angles between these reflections for the range of the Mach numbers of the curved shock investigated [33].

3.2 Comparison of shock propagation over solid and liquid surfaces

In order to compare the shock transition of curved shock reflection over solid and water surfaces, new experiments were carried out with the case-4 experimental model. For the new experiments, the shadowgraph images were taken at 145,251 fps with a resolution of 400×220 pixels and at 289 ns exposures. Figure 17 depicts the shadowgraph images showing the sequence of curved shock wave propagation over the solid wall and liquid surface (distance to interfaces from shock tube axis is kept at 58 mm). In this case also, the initial shock wave angle, the shock wave angle at transition, and the distance the shock wave travels before it transitions to IR have been computed from shadowgraph images for both the air–water interface and air–solid interface. It is observed from Fig. 17 that the unsteady shock wave reflection characteristics (the shock wave angle at the transition point and the distance the shock front traveled before it is transitioned to

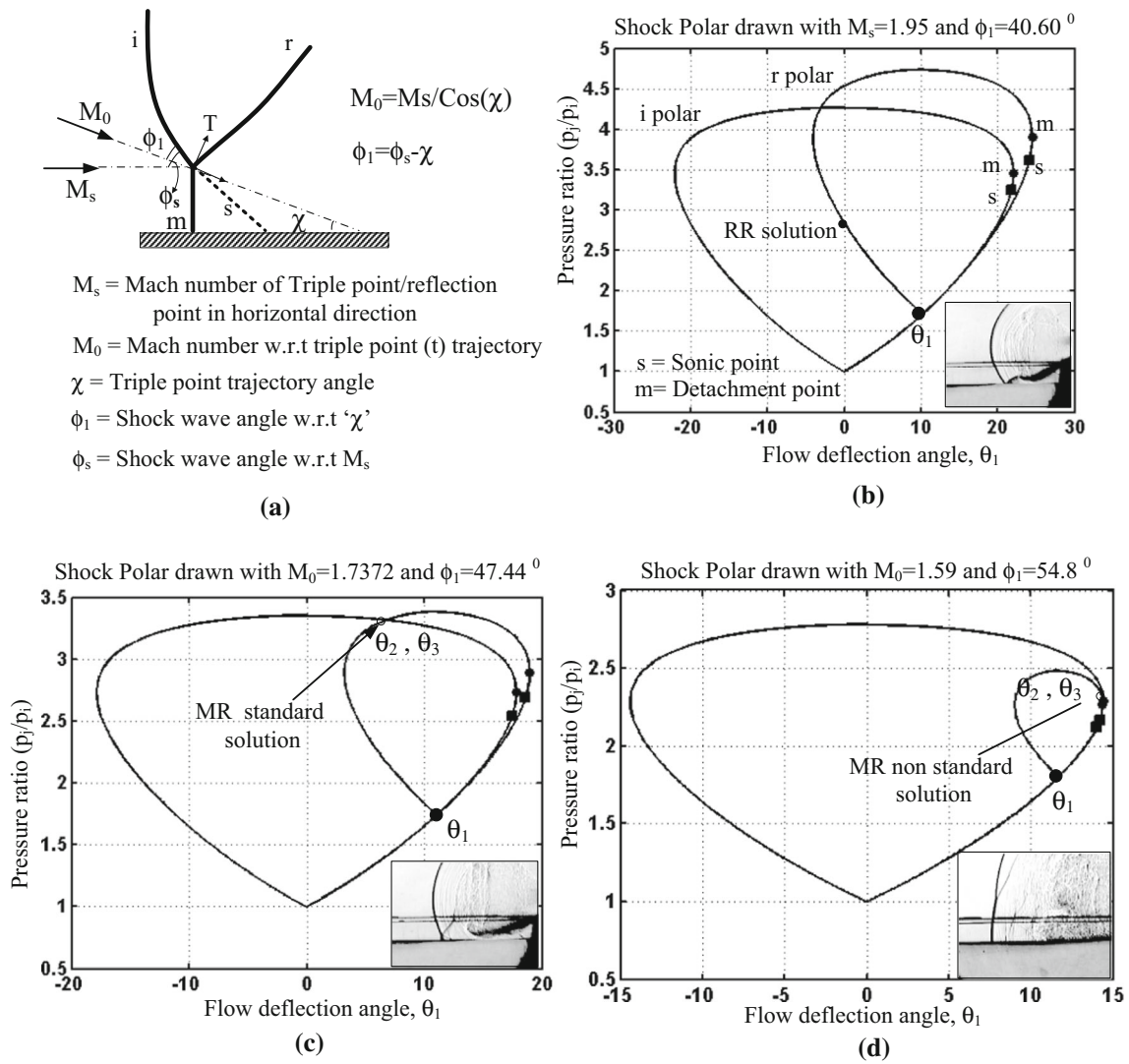


Fig. 15 Shock polar for the shock reflections at various instants (case-2). The shock polars are drawn with a quasi-steady assumption: **a** schematic showing typical IR configuration and nomenclatures, **b** shock polar at $t = 80 \mu\text{s}$, **c** shock polar at $t = 133.33 \mu\text{s}$, and **d** shock polar at $t = 300 \mu\text{s}$

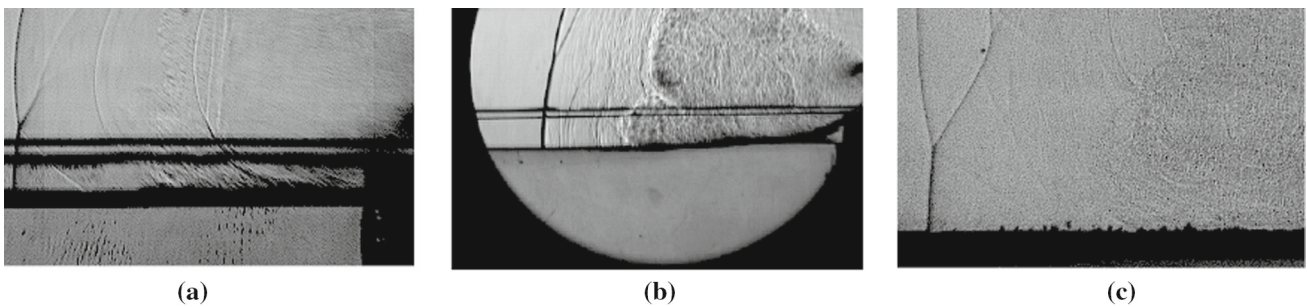


Fig. 16 Shadowgraph images showing the non-standard-type Mach reflection from various water-level cases: **a** case-1, **b** case-2, and **c** case-3

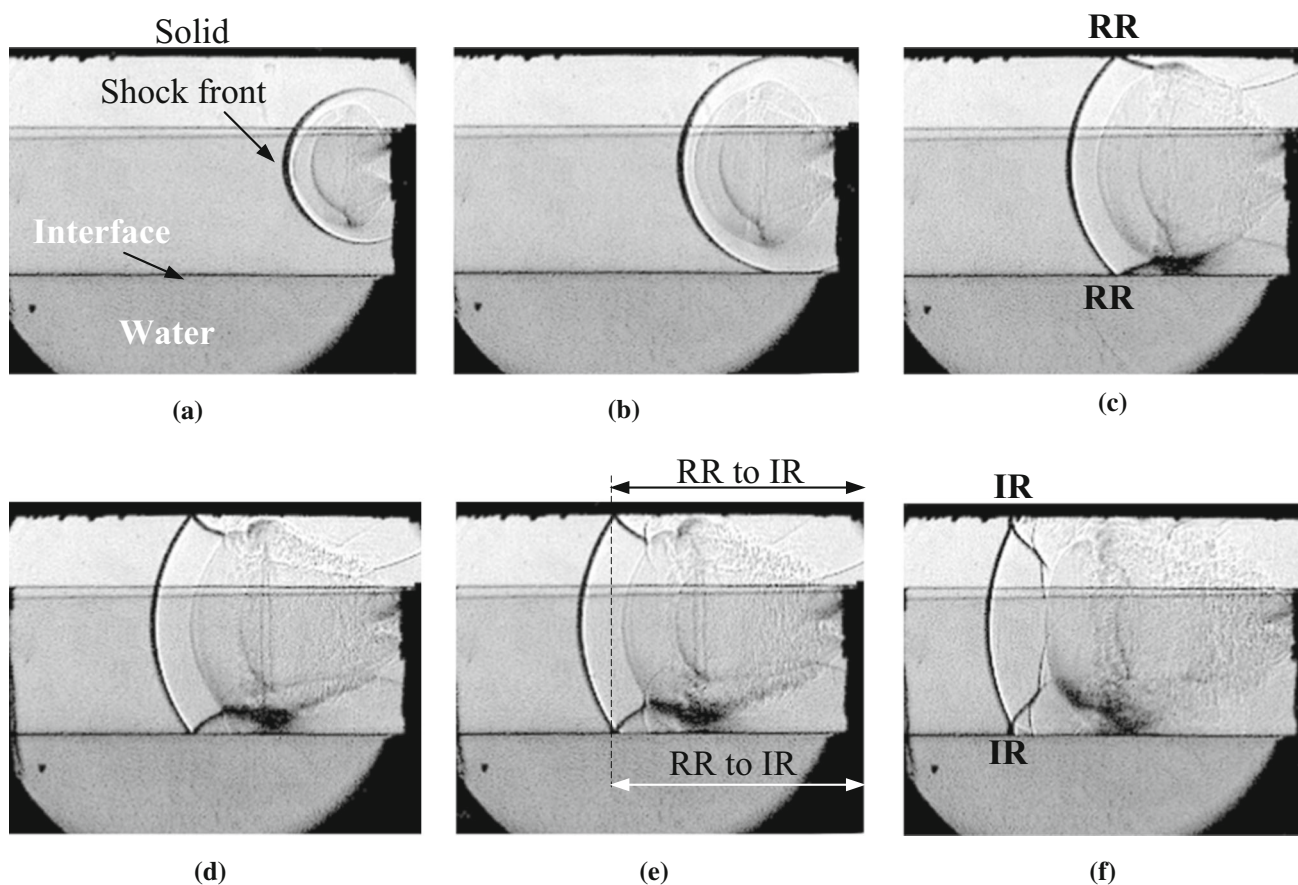


Fig. 17 Curved shock reflection characteristics over solid and liquid surface (case-4). Here $t = 0$ corresponds to the time instant at which the shock just emanates from the tube: **a** $t = 34.42 \mu\text{s}$, **b** $t = 68.86 \mu\text{s}$, **c** $t = 89.5 \mu\text{s}$, **d** $t = 117.04 \mu\text{s}$, **e** $t = 144.57 \mu\text{s}$, and **f** $t = 199.65 \mu\text{s}$

IR) are nearly the same for both the air–solid and air–water interfaces. This might be because the refracted shock wave energy is not that prominent in the present case and does not significantly affect the shock reflection characteristics at the air–water interface. However, this conclusion is made based on previous studies which reported that the refracted shock wave will be feeble compared to the reflected shock wave over an air–water interface [24,26]. This aspect is planned to be investigated in a future study by more elaborate underwater pressure measurements.

4 Conclusions

The present study investigated the reflection and refraction characteristics of a curved shock front as it slides along an air–water interface. The shock wave reflection and the transition are purely unsteady with both Mach number and shock wave angle varying. It is seen from the present study that a curved shock front sliding over the air–water interface transitions from a regular reflection to a standard Mach reflection (SMR). It is found that the transition conditions (RR \rightarrow SMR) do not show much variation with change in the

interface distance. The standard Mach reflection further transitions to a non-standard Mach reflection as it propagates further along the interface. The shock transition thus follows the path: RR \rightarrow Standard Mach Reflection \rightarrow Non-Standard Mach Reflection. It is also found that with the increase in the interface distance from the shock tube axis, the shock wave travels more distance along the interface before it transitions from RR to SMR. The shadowgraph images from the present study depicted the propagation of a sharp refracted shock wave also, into the water. The present study also reveals that the unsteady shock reflection over solid and liquid surfaces shows no noticeable difference in the shock transition angles.

Appendix

In the present study, the shock wave angle and shock Mach number were computed from the shadowgraph images through image processing. In order to determine the shock profile from the raw image, the Canny edge detection algorithm (using MATLAB platform) was used. From the edge detection algorithm, the pixel values at the shock front can be found. Figure 18a shows the raw image, and Fig. 18b shows

the corresponding processed image using the Canny algorithm. The pixel values from the processed image can then be used to locate the shock position at various time intervals. For the reconstruction of the shock profile, the pixel locations at the shock front need to be converted to their corresponding physical distance from a reference frame. This is done by computing the physical dimension represented by each pixel (millimeters per pixel) for a particular experiment. In order to compute the value of millimeters per pixel, the shadowgraph images of a measuring scale with a known length (38 mm width) were captured prior to each experiment. From this, the number of pixels representing the image of the measuring scale can be computed, which in turn can be used to compute the value of millimeters per pixel. In the present study, one pixel is found to represent a physical dimension of 0.76 mm.

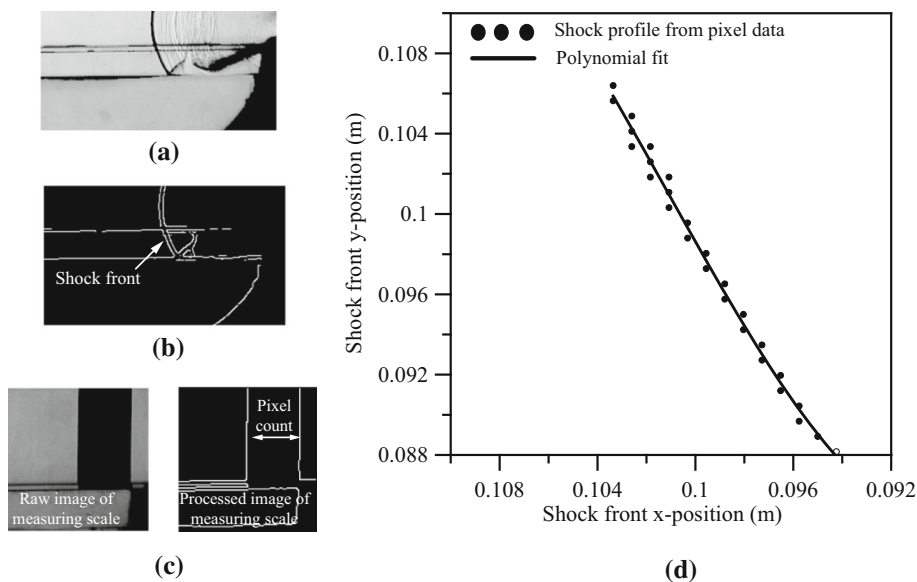
An illustration of this is shown in Fig. 18c. The position of the shock front is then computed by multiplying the pixel value at the shock front with the value of millimeters per pixel. A typical reconstructed shock profile for the experiment with the case-2 condition is shown in Fig. 18d. The shock speed (v) is then found by noting the shock propagation distance between two frames (by counting the change in pixel location of the shock front in the two frames) and the interframe time which is available from the frames per second (interframe time, $t = 1/\text{fps}$). From the shock speed, the shock wave Mach number can be easily computed ($M_s = v/c$). For determining the shock wave angle, the pixel locations at the shock front close to the interface are extracted from the images (shock front in the limit of only 3-pixel height are considered). A linear curve fitting was employed to reconstruct the small portion of the shock front close to the interface, which in turn can be used to determine the shock wave angle. It is expected that the linear curve fitting

assumption close to the interface is valid since an infinitesimal portion of any general curve can be represented as a linear curve.

In the present study, it is assumed that the shock front lies at the center point of the pixel representing the shock front. However, this consideration leads to an error of ± 0.5 pixels in the measurement since the shock front can be at any point in the pixel representing the shock front. This error was accounted for in the Mach number measurements from the images by computing the uncertainty in position determination from the images. The uncertainty in position determination from the images corresponds to the physical distance represented by ± 0.5 pixels. In order to estimate the repeatability and the error in shock wave angle measurements, the experiment for each water-level case was repeated at least three times. The shock wave angles are then measured from each of these experiments. The error in shock wave angle measurement is computed from the standard deviation from the measured values from each of these experiments.

The triple-point Mach number (M_s) and the triple-point trajectory have also been computed from image processing, as shown in Fig. 19. The value of M_s is computed by tracking the triple-point location at various time steps. The x -coordinate of the triple point at various time steps is tracked from the pixel values. From the x -coordinates, the distance moved by the triple point in the x -direction (x_1-x_2) can be computed, as shown in Fig. 19a and b. From this, the triple-point Mach number along the x -direction (M_s) can be computed as $M_s = \frac{\Delta x}{\Delta t a_s}$, where a_s is the acoustic speed upstream to the incident shock wave and Δt is the interframe time step. The incident shock angle with respect to the triple-point trajectory (ϕ_1) at each time step can be computed by reconstructing the incident shock profile and the triple-point trajectory using image processing. The triple-point trajectory

Fig. 18 Shock profile reconstruction using image processing (case-2): **a** raw shadowgraph image, **b** processed image using "Canny" edge detection algorithm, **c** millimeters-per-pixel computation from known reference length, and **d** reconstructed shock profile near the reflection point from the processed image



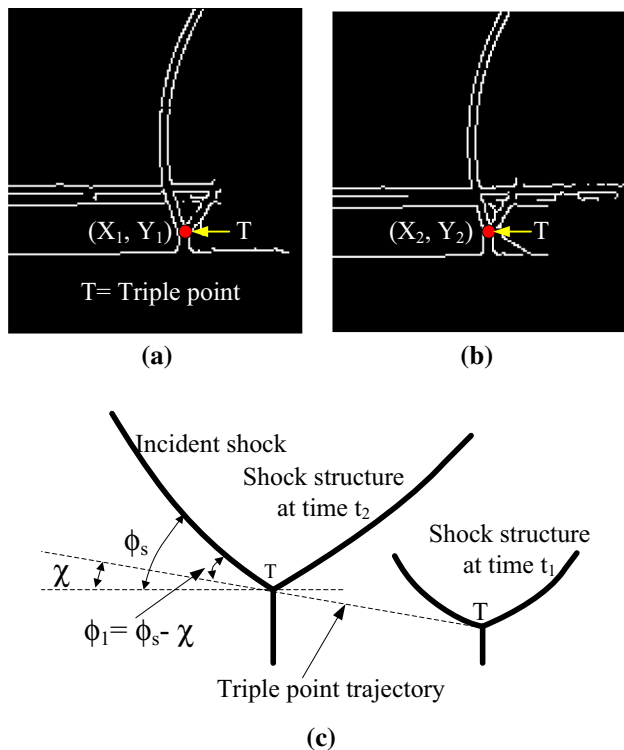


Fig. 19 Triple-point trajectory computation using image processing: **a** processed image at $t = 200 \mu\text{s}$, **b** processed image at $t = 213.33 \mu\text{s}$, and **c** schematic showing triple-point trajectory and various shock wave angles

can be reconstructed by computing the x - and y -coordinates of the triple point at various time instants. The slope of the triple-point trajectory at any particular time instant gives the angle χ with respect to the x -direction. Similarly, the shock wave angle (ϕ_s) with respect to the x -direction can be computed from the processed images. The difference between the angles ϕ_s and χ gives the incident shock angle with respect to the triple-point trajectory at a particular time instant. A schematic representation of this is shown in Fig. 19c.

Acknowledgements The authors gratefully acknowledge the financial support for this project from the INSPIRE Grant (Grant No. DST/INSPIRE/04/2018/001780), Department of Science and Technology (DST), India.

Funding Funding was provided by INSPIRE Grant, Department of Science and Technology, India (Grant No. IFA18-ENG251).

Data Availability The data that support the findings of this study are available from the corresponding author upon reasonable request.

References

- Von Neumann, J.: Refraction, intersection and reflection of shock waves. NAVORD Report 203-245 (1945)
- Hornung, H.G., Oertel, H., Sandeman, R.J.: Transition to Mach reflexion of shock waves in steady and pseudosteady flow with and without relaxation. *J. Fluid Mech.* **90**(3), 541–560 (1979). <https://doi.org/10.1017/S002211207900238X>
- Semenov, A.N., Berezkina, M.K., Krassovskaya, I.V.: Classification of pseudo-steady shock wave reflection types. *Shock Waves* **22**, 307–316 (2012). <https://doi.org/10.1007/s00193-012-0373-z>
- Delius, M.: Medical applications and bioeffects of extracorporeal shock waves. *Shock Waves* **4**, 55–72 (1994). <https://doi.org/10.1007/BF01418569>
- Flores, J., Holt, M.: Shock wave interactions with the ocean surface. *Phys. Fluids* **25**, 238–246 (1982). <https://doi.org/10.1063/1.863753>
- Ben-Dor, G.: *Shock Wave Reflection Phenomena*, 2nd edn. Springer, Berlin (2007). <https://doi.org/10.1007/978-3-540-71382-1>
- Henderson, L.F., Lozzi, A.: Experiments on transition of Mach reflexion. *J. Fluid Mech.* **68**(1), 139–155 (1975). <https://doi.org/10.1017/S0022112075000730>
- Ben-Dor, G.: A reconsideration of the three-shock theory for a pseudo-steady Mach reflection. *J. Fluid Mech.* **181**, 467–484 (1987). <https://doi.org/10.1017/S0022112087002179>
- Takayama, K., Ben-Dor, G., Gotoh, J.: Regular to Mach reflection transition in truly nonstationary flows—influence of surface roughness. *AIAA J.* **19**, 1238–1240 (1981). <https://doi.org/10.2514/3.7852>
- Ram, O., Geva, M., Sadot, O.: High spatial and temporal resolution study of shock wave reflection over a coupled convex–concave cylindrical surface. *J. Fluid Mech.* **768**, 219–239 (2015). <https://doi.org/10.1017/jfm.2015.80>
- Kleine, H., Timofeev, E., Hakkaki-Fard, A., Skews, B.: The influence of Reynolds number on the triple point trajectories at shock reflection off cylindrical surfaces. *J. Fluid Mech.* **740**, 47–60 (2014). <https://doi.org/10.1017/jfm.2013.634>
- Ben-Dor, G., Takayama, K.: Analytical prediction of the transition from Mach to regular reflection over cylindrical concave wedges. *J. Fluid Mech.* **158**, 365–380 (1985). <https://doi.org/10.1017/S0022112085002695>
- Itoh, S., Okazaki, N., Itaya, M.: On the transition between regular and Mach reflection in truly non-stationary flows. *J. Fluid Mech.* **108**, 383–400 (1981). <https://doi.org/10.1017/S0022112081002176>
- Geva, M., Ram, O., Sadot, O.: The regular reflection → Mach reflection transition in unsteady flow over convex surfaces. *J. Fluid Mech.* **837**, 48–79 (2018). <https://doi.org/10.1017/jfm.2017.835>
- Vignati, F., Guardone, A.: Transition from regular to irregular reflection of cylindrical converging shock waves over convex obstacles. *Phys. Fluids* **29**, 116104 (2017). <https://doi.org/10.1063/1.4989384>
- Kleine, H., Timofeev, E., Takayama, K.: Reflection of blast waves from straight surfaces. In: Jiang, Z. (ed.) *Shock Waves*. Springer, Berlin (2005)
- Dewey, J., Mcmillin, D., Classen, D.: Photogrammetry of spherical shocks reflected from real and ideal surfaces. *J. Fluid Mech.* **81**(4), 701–717 (1977). <https://doi.org/10.1017/S0022112077002304>
- Hu, T.C.J., Glass, I.I.: Blast wave reflection trajectories from a height of burst. *AIAA J.* **24**, 607–610 (1986). <https://doi.org/10.2514/3.9314>
- Henderson, L.F., Ma, J.H., Sakurai, A., Takayama, K.: Refraction of a shock wave at an air–water interface. *Fluid Dyn. Res.* **5**, 337–350 (1990). [https://doi.org/10.1016/0169-5983\(90\)90003-H](https://doi.org/10.1016/0169-5983(90)90003-H)
- Henderson, L.F.: On the refraction of shock waves. *J. Fluid Mech.* **198**, 365–386 (1989). <https://doi.org/10.1017/S0022112089000170>
- Henderson, L.F.: On shock impedance. *J. Fluid Mech.* **40**(4), 719–735 (1970). <https://doi.org/10.1017/S002211207000040X>
- Borisov, A.A., Gelfand, B.E., Sherpanev, S., Timofeev, E.I.: Mechanism for mixture formation behind a shock sliding over a fluid

- surface. *Combust. Explos. Shock Waves* **17**, 86–93 (1981). <https://doi.org/10.1007/BF00798146>
23. Teodorczyk, A., Shepherd, J.E.: Interaction of a shock wave with a water layer. Technical Report FM2012-002, California Institute of Technology, USA (2012)
 24. Rodriguez, V., Jourdan, G., Marty, A., Allou, A., Parisse, J.D.: Planar shock wave sliding over a water layer. *Exp. Fluids* **57**, 125–130 (2016). <https://doi.org/10.1007/s00348-016-2217-6>
 25. Takayama, K., Ben-Dor, G.: Pseudo-steady oblique shock wave reflections over water wedges. *Exp. Fluids* **8**, 129–136 (1989). <https://doi.org/10.1007/BF00195786>
 26. Wan, Q., Jeon, H., Deiterding, R., Eliasson, V.: Numerical and experimental investigation of oblique shock wave reflection off a water wedge. *J. Fluid Mech.* **826**, 732–758 (2017). <https://doi.org/10.1017/jfm.2017.452>
 27. Kleine, H., Timofeev, E., Voinovich, P., Takayama, K.: Blast wave reflection from solid, liquid, and gaseous surfaces. In: Lu, F. (ed.) Proceedings on 23rd ISSW, Paper 1903, CD-ROM Proceedings (2002)
 28. Sembiana, S., Liverts, M., Tillmark, N., Apazidis, N.: Plane shock wave interaction with a cylindrical water column. *Phys. Fluids* **28**, 056102 (2016). <https://doi.org/10.1063/1.4948274>
 29. Hosseini, H., Moosavi-Nejad, S., Akiyama, H., Menezes, V.: Shock wave interaction with interfaces between materials having different acoustic impedances. *Appl. Phys. Lett.* **104**, 103701 (2014). <https://doi.org/10.1063/1.4867883>
 30. Colella, P., Henderson, L.F.: The von Neumann paradox for the diffraction of weak shock waves. *J. Fluid Mech.* **213**, 71–94 (1990). <https://doi.org/10.1017/S0022112090002221>
 31. Vasilev, E.I., Kraiko, A.N.: Numerical simulation of weak shock diffraction over a wedge under the von Neumann paradox conditions. *USSR Comput. Math. Math. Phys.* **39**, 1335 (1999)
 32. Guderly, K.G.: Consideration of the structure of mixed subsonic-supersonic flow patterns. Technical Report F-TR-2168-ND, Wright Field, USA (1947)
 33. Vasilev, E.I., Elperin, T., Ben-Dor, G.: Analytical reconsideration of the von Neumann paradox in the reflection of a shock wave over a wedge. *Phys. Fluids* **20**, 046101 (2008). <https://doi.org/10.1063/1.2896286>

Publisher's Note Springer Nature remains neutral with regard to jurisdictional claims in published maps and institutional affiliations.

Springer Nature or its licensor holds exclusive rights to this article under a publishing agreement with the author(s) or other rightsholder(s); author self-archiving of the accepted manuscript version of this article is solely governed by the terms of such publishing agreement and applicable law.